A natural-gas fuel processor for a residential fuel cell system

H. Adachi [a], S. Ahmed [b], S.H.D. Lee [b], D. Papadias [b,*], R.K. Ahluwalia [b],
J.C. Bendert [b], S.A. Kanner [b], Y. Yamazaki [c]

[a] *The Japan Institute of Energy, Tokyo, Japan*
[b] *Argonne National Laboratory, Argonne, IL, United States*
[c] *Tokyo Institute of Technology at Nagatsuta, Yokohama, Japan*

ABSTRACT

A system model was used to develop an autothermal reforming fuel processor to meet the targets of 80% efficiency (higher heating value) and start-up energy consumption of less than 500 kJ when operated as part of a 1-kWe natural-gas fueled fuel cell system for cogeneration of heat and power. The key catalytic reactors of the fuel processor – namely the autothermal reformer, a two-stage water gas shift reactor and a preferential oxidation reactor – were configured and tested in a breadboard apparatus. Experimental results demonstrated a reformate containing ∼48% hydrogen (on a dry basis and with pure methane as fuel) and less than 5 ppm CO. The effects of steam-to-carbon and part load operations were explored.

© 2008 Elsevier B.V. All rights reserved.

1. Introduction

Fuel cell-based cogeneration systems are attractive for households because of the balanced heat and power output achievable from these environmentally clean and efficient devices. Fuel cell power systems are being deployed in Japan to meet or supplement the heat and electric power needs of private residences [1,2]. The ability to operate fuel cell systems with an infrastructure fuel such as natural gas, liquefied petroleum gases, or kerosene provides a tremendous advantage for distributed power generation. These stand-alone fuel cell systems typically convert the fuel in a fuel processor that delivers the fuel cell quality hydrogen to the fuel cell. The Japan Institute of Energy has established a correlation between the volume of units deployed and their unit cost, shown in Table 1, where such systems are economically attractive and can compete with existing sources of heat and power, namely electric power from the grid or fuel burners for heat. The correlation indicates that technological advancements are needed to meet the long-term (year 2016) cost target of $4000 kWe^{-1}.

The fuel cell systems currently deployed in the Japanese residential demonstration programs use steam reformers to convert the fuels [1,2]. This approach yields high concentrations of hydrogen for the fuel cell stack, and these systems can operate efficiently at steady state at the design point. However, the duty cycle of the residential cogeneration systems consist of daily start–stop cycling, and load that varies between 30 and 100% of capacity. Steam reformers with their large thermal mass, require considerable time and energy (fuel) to warm up to operating temperatures, and are slow to respond during load transitions. It is anticipated that, compared to a steam-reformer, an autothermal reformer (ATR)-based system can significantly reduce the thermal mass of the fuel processor, since the ATR operates at much higher (1–2 orders of magnitude) space velocities. Furthermore, ATRs have been demonstrated to have fast start-up performance [3] and can be more responsive to load changes. With less fuel energy wasted at start-up, these systems are expected to be more energy efficient over their lifecycle – an appropriate measure of a key performance metric driving the development of these distributed heat and power applications.

The purpose of this paper is to discuss the development of a natural-gas fueled ATR-based fuel processing system (FPS) as a part of a 1-kWe fuel-cell cogeneration system (FCS), for residential applications. Some key requirements of this system are [1–3]

- The FPS is to be fueled by natural gas with an average composition of 88% CH_4, 5.8% C_2H_6, 4.5% C_3H_8 and 1.7% C_4H_{10}.
- The FPS must maintain greater than 80% efficiency (based on the fuel's higher heating value (HHV)) over its operating range of 30–100% of capacity.

* Corresponding author at: Chemical Sciences and Engineering Division, 9700 S. Cass Avenue, Argonne, IL 60439, United States. Tel.: +1 630 252 3206; fax: +1 630 972 4523.

E-mail address: papadias@anl.gov (D. Papadias).

Table 1
Deployed volume and costs of residential fuel cell systems in Japan.

	Fiscal year			
	2008	2009	2012	2016
Anticipated volume of deployed units ($\times 10^3$)	1.1	5	70	>300
Required unit cost ($\times 10^3$)				
By using existing technology	>$30	$21	$12	
By using advanced technology			$8	$4

- The fuel cell system should generate the electric power at greater than 31% electric efficiency (HHV).
- The start-up energy consumed by the FCS must be less than 3.6 MJ (1 kWh) per start.

2. The fuel cell system configurations

GCTool, a fuel cell system design and analysis code [4], was used to identify two FPS configurations that can meet the efficiency and start-up energy targets and are self-sufficient in terms of water used. The first configuration, termed C1, relies on passive non-phase-change devices to recover process water and supply steam to the ATR. It offers higher thermal efficiency than the current state-of-the-art practice as the condenser that produces low-grade heat, which is difficult to utilize because of a pinch-point temperature limitation, has been eliminated. The operating steam-to-carbon (S/C) ratio in the ATR, however, is constrained by the fuel-cell stack temperature and by the pressure drops in the FPS (34 kPa or 5 psi) and in the downstream components. The second configuration, termed C2, overcomes this limitation by raising additional steam using the waste heat in the burner effluent. The S/C in C2 is higher, resulting in improved FPS efficiency but the system is more complex than C1.

Fig. 1 shows the thermal integration of the fuel processor with the downstream components in the configuration C1. At reference conditions, the reformate leaving the ATR is first used to preheat the process air to 600 °C in a high-temperature recuperator and then is quenched with steam to the inlet temperature of the first-stage water gas shift (WGS) reactor. The steam quench increases the overall S/C in the fuel processor to 4.9. The important parameters for the reference system are summarized below.

ATR: 750 °C (at exit), 34 kPa, 3% heat loss
   Air feed at 550 °C, 77 °C $T_{dewpoint}$, ΔP = 34 kPa (5 psi)
   Fuel feed at 80 °C, 77 °C $T_{dewpoint}$, ΔP = 34 kPa (5 psi)
   WGS reactor, two stages, with inlet temperatures of 375 °C and 300 °C
   PrOx reactor, with inlet temperature of 100 °C, 0.2 ppm CO at exit

Air management
   Anode air blower: 34 kPa head, 60% efficiency
   Cathode air blower: 13.7 kPa head, 60% efficiency

Water management
   Enthalpy wheel humidifier (EWH) for air humidification [5]
   Membrane humidifier (MH) for fuel humidification [5]
   Stack condensate is recovered

Fuel cell stack (FCS) module
   80% fuel utilization (FU), 50% air utilization (OU)
   Air preheated to 80 °C, 77 °C $T_{dewpoint}$
   Reformate at 80 °C, >77 °C $T_{dewpoint}$
   0.75 V cell voltage at rated power
   80 °C stack temperature
   13.7 kPa (2 psi) total pressure drop in stack and downstream components

Parasitic losses
   90% DC/AC inverter efficiency
   95% DC/DC converter efficiency
   95% blower motor efficiency
   60% blower efficiency

Table 2
Performance of FPS in C1 and C2 configurations.

	C1	C2	C2*
ATR temperature	750 °C	750 °C	750 °C
S/C (ATR)	1.65	2.21	6.20
S/C (FPS)	4.9	5.5	6.2
%CO (ATR)	10.2	8.8	7.5
%CH$_4$ (ATR)	0.05	0.03	0.01
Efficiency (HHV)			
FPS (%)	88.4	88.5	88.5
FCS (%)	31.0	31.1	31.1
Total (%)	82.6	82.6	82.6
Heat recovery			
Stack radiator (W)	1300	1300	1300
Anode cooler (W)	70	160	270
Burner HX (W)	200	100	0
Desuperheater (W)	90	90	90
Condenser (W)	0	0	0
Total (W)	1660	1660	1660

Table 2 compares the thermal efficiencies of the FPS in configurations C1 and C2, the electric efficiencies of FCS, the combined thermal and electric efficiencies, and the heat loads on the heat exchangers. Also included in Table 2 is the performance of C2* in the limit of maximum S/C that is possible in ATR.

Fig. 2 shows the temperatures and the concentrations of CO and H$_2$ exiting the components in the FPS. Humidified natural gas and process air enter the ATR at a mixing-cup temperature of 506 °C. The reformate exits the ATR at 750 °C, is cooled to 519 °C in the high-temperature recuperator (HRC), and is then further cooled to 375 °C by steam injection. The WGS reaction is mildly exothermic, so that the reformate temperature rises to 429 °C after WGS1. The reformate is cooled to 300 °C in the heat exchanger HW2. There is a 5 °C temperature rise in WGS2. The heat exchanger HP1 cools the reformate to 120 °C – the target inlet temperature for the PrOx reactors. The reformate temperature rises in each of the PrOx reactors and is cooled back down in the heat exchangers (HP2 and HAC) as needed for the next component. The dew point temperature of the reformate leaving PrOx is >77 °C so that no further humidification is required to meet the >90% RH target. The reformate is cooled to 80 °C in the heat exchanger HP1.

The heat exchangers HW2 and HP1 are cooled using the process water that is converted to steam to quench the reformate to 375 °C at the inlet to WGS1.

The CO concentration in the reformate is 10.4% at the exit of the ATR (on a dry basis). The WGS reactors reduce the CO concentration to 1.1% in the first stage and to 0.3% in the second stage. The PrOx reactors further reduce the CO concentration to 2 ppm.

The H$_2$ concentration in the reformate is 39.8% at the exit of the ATR (on a dry basis). The WGS reactors raise the H$_2$ concentration to 45.0% in the first stage and to 45.9% in the second stage. The H$_2$ concentration decreases in the preferential oxidation reactors (PrOx) to 44.9%.

The two-stage PrOx reactor in the reference system has an overall CO selectivity of 55%, operates at a stoichiometry of 1.1 (i.e., O-to-CO ratio) and achieves a CO selectivity of 63% (i.e., 37% of added O$_2$ goes into oxidizing H$_2$ rather than CO). The second stage operates at a stoichiometry of 2.2 and achieves a CO selectivity of 44%. The overall CO stoichiometry in the two-stage PrOx is 1.8 [6].

We have estimated the start-up energy for the FPS. At 100% heat transfer effectiveness, the amount of fuel energy needed for FPS start-up is 430 kJ, with 280 kJ required to heat the catalytic reactors, 40 kJ for the heat exchangers, and 110 kJ to heat 500 g of process water to the stack temperature of 80 °C. Fig. 3 shows
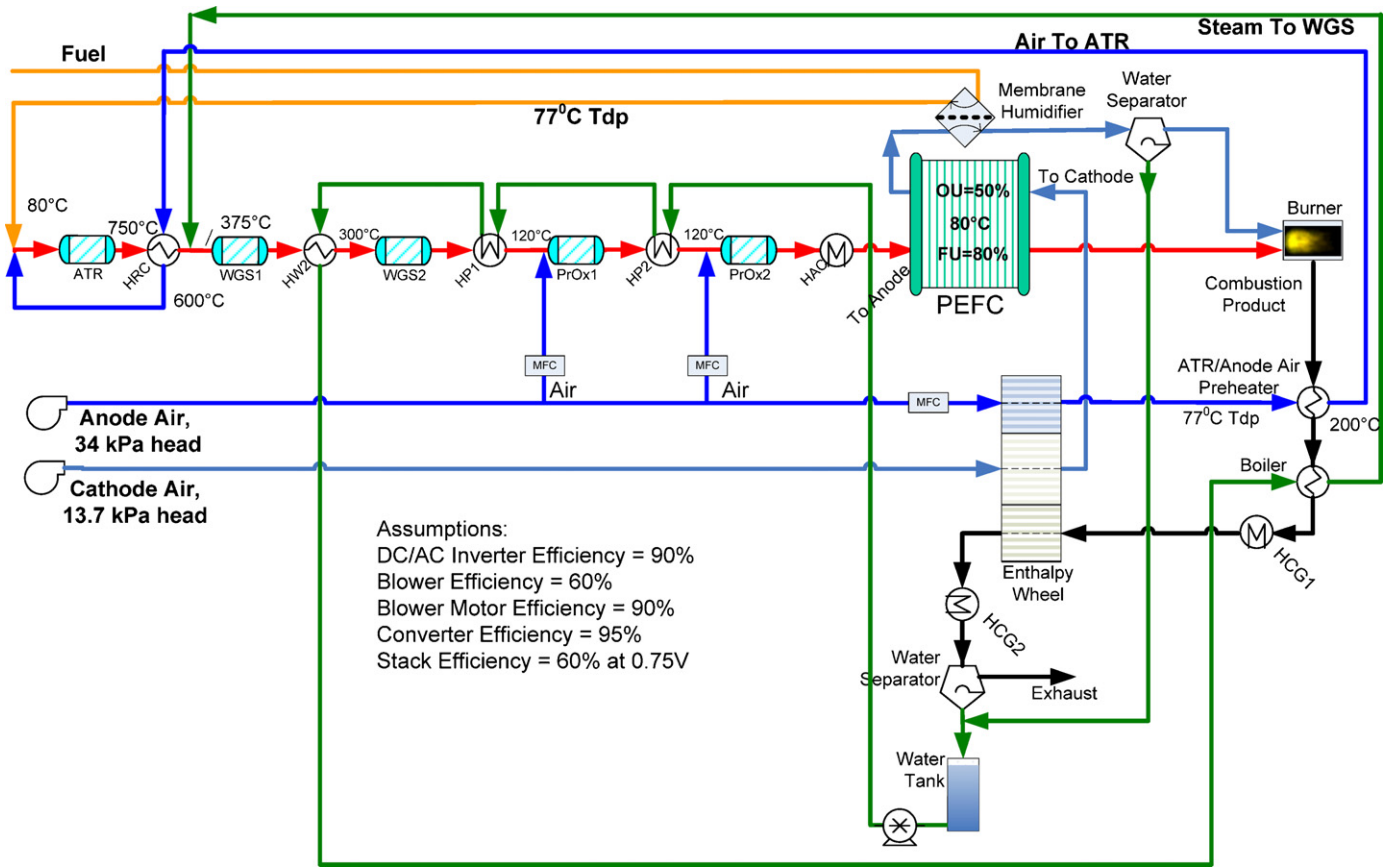
Fig. 1. Fuel cell system (FCS) configuration C1.

a distribution of the start-up energy needs of each fuel processor component. As a comparison, the fuel energy consumed in generating 8 kWh of electricity/day is 83,600 kJ at 31.2% electrical efficiency. Thus, in a daily cycle that involves one start-up and shutdown and

8 kWh of electricity demand, the start-up energy is only a small fraction of the fuel energy consumed in generating the electric power. Thus, it would be advantageous to increase the system efficiency, for example, by using a lower approach temperature in the
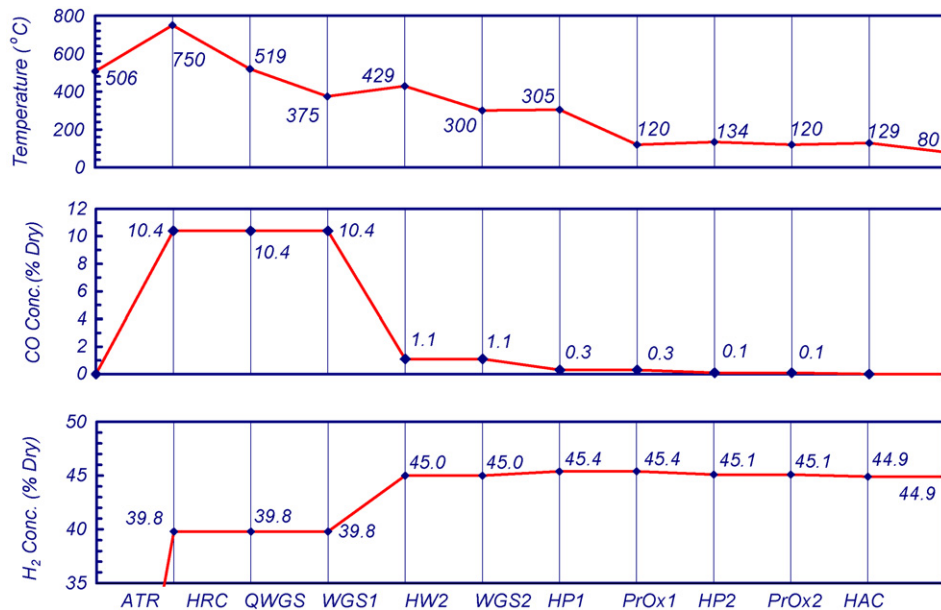
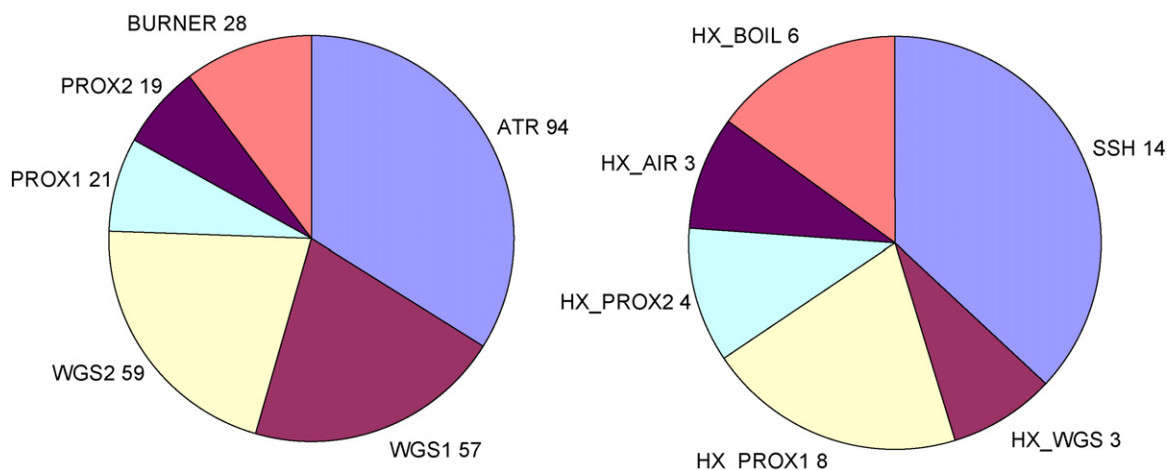**Fig. 2.** Temperature and concentration profiles across the fuel processor system.

Fig. 3. Start-up energy needs (kJ) for the fuel processor components.

recuperator (which would lead to a lower O_2/C in the ATR), at the expense of a slightly greater start-up energy consumption (bulkier heat exchanger).
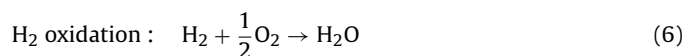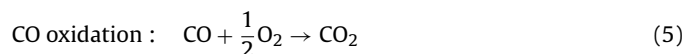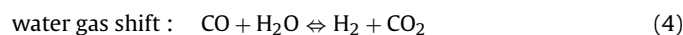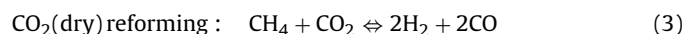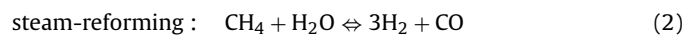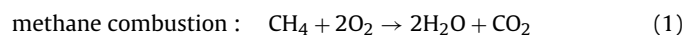
2.1. Catalytic reactors in the fuel processor

2.1.1. The autothermal reformer

For the ATR, a noble-metal catalyst was preferred because of the need to expose the catalyst to air during the daily shutdowns. The lower cost nickel-based catalysts require in situ reduction, tend to be pyrophoric if the reduced nickel is exposed to air, and have a greater tendency to form carbonaceous species. Rhodium supported on metal oxides was selected as the catalyst because it has been shown to have significantly higher activity and hydrogen selectivity for reforming than other noble-metal catalysts [7]. In partial oxidation of methane, for example, conversion of methane approaches thermodynamic equilibrium yields with a Rh catalyst even at short contact times with little or no macroscopic carbon deposition being observed. Based on literature data and in-house experience, we selected La-stabilized alumina as the support for Rh since (1) lanthanum as a basic oxide supports gasification of carbon in reforming reactions; (2) lanthanum forms a lanthanum aluminate ($LaAlO_x$) at the surface which has been shown to prevent the migration of Rh into the support. Further, we selected a metal (40 ppi FeCrAlY) foam rather than ceramic monoliths as the support for the $Rh/La-Al_2O_3$ catalyst because of its higher thermal conductivity and superior ability to disperse heat in the radial direction [8]. We expect the foam support to be more effective than ceramic monoliths in achieving uniformity of temperature and avoiding formation of hot or cold spots due to imperfect mixing of the reactants. Furthermore, foams typically achieve an order of magnitude higher heat and mass-transfer rates than monoliths, yet have comparable surface areas to provide good catalyst utilization. Foams, however, are associated with higher pressure drops than honeycomb monolithic supports. Foams may need careful sizing to optimize mass- and heat transfer rates while keeping pressure drop losses to a minimum [9].

A 1D, heterogeneous kinetic model was developed to simulate the autothermal reforming of methane and size the reactor. The model, including heat-losses through the reactor wall, is described in more detail in a previous work [10]. Briefly, the model includes the species mass balances and the energy balances for the gas and solid phase respectively with appropriate correlations for the metal foam support (40 ppi FeCrAlY) [9,11]. Kinetics for the autothermal reforming of methane on Rh-based catalysts was based on the work by Tavazzi et al. [12]. An indirect kinetic scheme was proposed by

Tavazzi et al. [12], reactions (1)–(6), consisting of primary deep CH_4 oxidation (1) followed by secondary reactions of steam (2) and CO_2 reforming (3). In addition, the reaction pathways also included the water gas shift reaction (4) and the oxidation of CO (5) and H_2 (6) in parts of the reactor where oxygen is still available

$$\text{methane combustion}: \quad CH_4 + 2O_2 \rightarrow 2H_2O + CO_2 \tag{1}$$

$$\text{steam-reforming}: \quad CH_4 + H_2O \Leftrightarrow 3H_2 + CO \tag{2}$$

$$CO_2\,(\text{dry})\,\text{reforming}: \quad CH_4 + CO_2 \Leftrightarrow 2H_2 + 2CO \tag{3}$$

$$\text{water gas shift}: \quad CO + H_2O \Leftrightarrow H_2 + CO_2 \tag{4}$$

$$\text{CO oxidation}: \quad CO + \frac{1}{2}O_2 \rightarrow CO_2 \tag{5}$$

$$\text{H}_2 \text{ oxidation}: \quad H_2 + \frac{1}{2}O_2 \rightarrow H_2O \tag{6}$$

Assuming adiabatic conditions, Fig. 4 shows calculated steady-state species and temperature profiles in the ATR reactor. The reactor is divided into two sections, a catalyst section and an inlet section comprising of uncoated foam. The inlet section distributes the momentum of a high velocity reactant mix entering the ATR section from a static mixer to achieve a uniform flow rate into the catalyst section. Here, the results are shown for the C1 case with $S/C = 1.65$, $O_2/C = 0.52$, and inlet reactant feed temperature of 475 °C. The gas-hourly space velocity and catalyst mass (in catalyst zone) is 30,000 h^{-1} and 0.2 g cm^{-3}, respectively.

According to the model, there are two important regions in the bed. In the front of the catalytic bed, we see the effects of deep oxidation of methane, seen in Fig. 4 as a sharp drop in oxygen concentration and accompanied by a large adiabatic temperature rise within the first 10% of the bed. Some reforming does occur in this region, but the oxidation rate of methane is significantly higher than the rates of the endothermic reforming reactions, resulting in a net temperature increase. The deep oxidation of methane to carbon dioxide and water is also evident by the net increase in water formation immediately at the front of the bed, as shown in Fig. 4. As most of the oxygen is consumed, reforming reactions (primarily steam reforming) rapidly cool the remaining volume of the reactor bed forming CO and H_2 in large quantities.

The occurrence of the maximum temperature upstream the catalyst section (hot-spot) is a result of competing exothermic and endothermic reactions. The solid peak temperature, which is close to 960 °C, is of concern as the catalyst may sinter and deactivate over time at this high temperature [13]. Numerical experiments were performed to investigate parameters that can minimize the
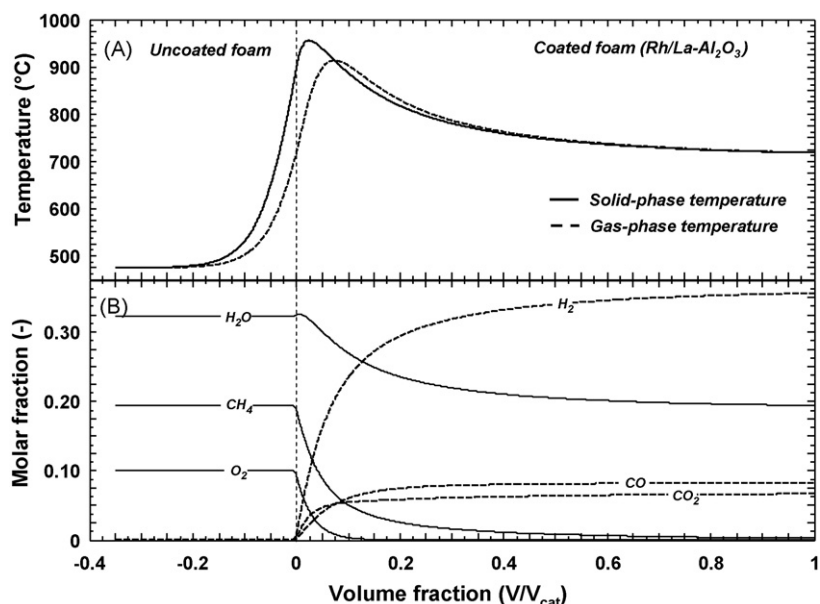
Fig. 4. Calculated temperature (A) and gas-phase species profiles (B) in the ATR reactor. Results shown for case C1 (S/C = 1.65, O_2/C = 0.52, T_{inlet} = 475 °C). GHSV = 30,000 h^{-1}, catalyst mass = 0.2 g cm^{-3}.

hot-spot formation at the front of the catalyst and explore various design options for the ATR. At first, the effect of the S/C ratio on the temperature profile was studied by varying the S/C from 1.4 to 2.8, while keeping all other parameters constant. The peak temperatures near the reactor inlet were slightly reduced at the higher S/C ratios, as shown in Fig. 5. The temperature at the exit of the bed decreased as well, albeit less steeply than the front. The temperature reduction was mainly due to the dilution effect of the additional steam, and to a smaller extent due to the endothermicity of the additional steam reforming reaction caused. A 70 °C temperature reduction could be achieved with a doubling of the steam content (S/C increased from 1.4 to 2.8). The interval of interest however is only between S/C ratios of 1.65 and 2.2, corresponding to case scenarios C1 and C2. The latter case represents a variant condition where it may be possible to operate the ATR at a higher steam-to-carbon ratio of 2.2 with good system efficiency. The reduction in peak temperature between the two cases is only 30 °C and the
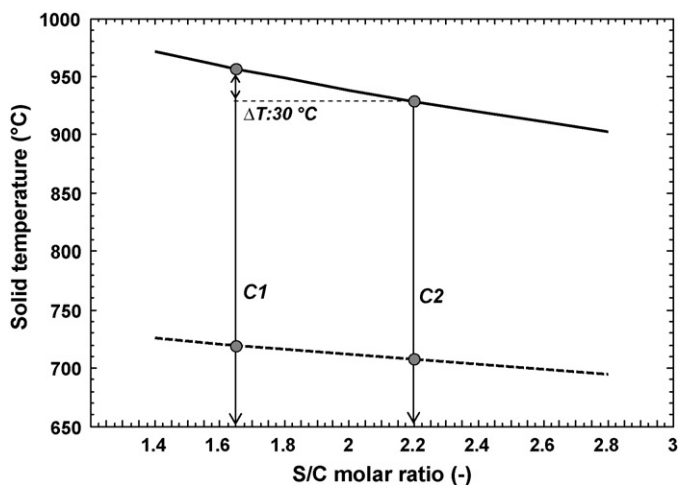
C2 conditions may not necessarily provide significant advantages in lowering the catalyst hot-spot. The conversion did not change appreciably between the two case scenarios. Higher steam content in the inlet feed increases methane conversion as the equilibrium of the steam reforming reaction (2) shifts to the product side. However, the higher S/C ratio tends to reduce the ATR temperature along the reactor bed and favored methane formation, equilibrium in Eqs. (2) and (3) shifts to the product side at lower temperatures. This did offset the gain in conversion at the higher S/C ratios.

The effect of space velocity was investigated to determine the effects of different turn-down ratios for the fuel processor. Fig. 6 shows the calculated effect of space velocity on the solid-phase temperatures in the reactor, and on fuel conversion. The results are shown for the C1 case. Decreasing the space velocity decreased the solid peak temperature gradually while increasing the conversion
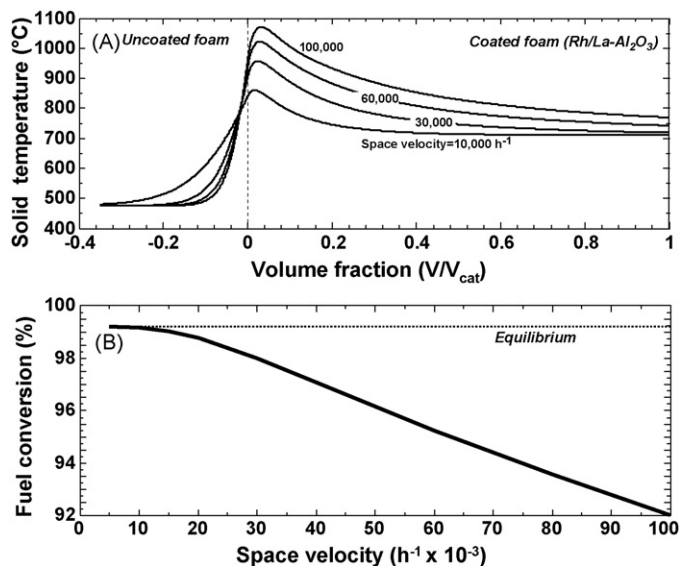

Fig. 5. Catalyst temperatures in the ATR as function of S/C ratio. Solid line = peak temperature, dashed line = exit reactor temperature. O_2/C = 0.52, T_{inlet} = 475 °C. GHSV = 30,000 h^{-1}, catalyst mass = 0.2 g cm^{-3}. Corresponding C1 and C2 conditions are shown on the graph (S/C = 1.65 and 2.2).

Fig. 6. (A) Solid-phase temperatures in the ATR bed at different space velocities. (B) Methane fuel conversion as function of space velocity. S/C = 1.65, O_2/C = 0.52, T_{inlet} = 475 °C. Catalyst mass = 0.2 g cm^{-3}.

to approach the equilibrium value. At high flow-rates, convective heat-transfer dominates and the cooling effect is the result of reforming reactions and energy transfer from the solid- to the gas-phase. As the flow-rate decreases, conductive heat-transfer starts to become important and disperses the heat-release in the front of the catalyst section back to the uncoated foam. At the lowest space velocity ($10,000\,h^{-1}$) the solid phase and gas phase almost approaches thermal equilibrium and a significant amount of heat is conducted back to the uncoated foam lowering the peak-temperature to 850 °C.

Using a blank foam prior to the catalyst section as a means to disperse the peak solid temperature at low space velocities appears to be a viable design option to reduce the peak temperature. However, an oversized reactor would lose too much heat when operating at low processing rates and, consequently, the fuel conversion would decline. An oversized reactor also adds to the cost of the catalyst, especially when it is an expensive metal such as rhodium.

The above numerical analysis was used to design the ATR reactor. We decided to design the ATR reactor at a space velocity of $30,000\,h^{-1}$ at 100% capacity. The calculated conversion at that point is sufficiently high, but the high temperature at the front edge of the catalyst poses a durability concern. To maintain high catalyst durability and the high activities achievable at elevated temperatures, we opted to use two different catalyst sections in the ATR. In the first section (15–20%) of the ATR reactor, where temperatures are too high for the use of a noble-metal catalyst, a hexa-aluminate type of catalyst was proposed. This would be followed by the Rh catalyst in the downstream section where temperatures below 900 °C are expected. Hexa-aluminate related catalysts have been proposed as material of high heat resistance especially in the research of high-temperature catalytic combustion [14–16]. These compounds have unique layer crystal structure consisting of alternate stacking of a spinel block and monoatomic layer of large cations such as Ba, Sr, or La which minimize crystal growth even at high temperatures. They retain relatively high surface areas $>20\,m^2\,g^{-1}$ even at temperatures of more than 1200 °C. There has been some renewed interest in the literature for those materials in the use of partial oxidation of methane because of their durability [17–20]. While their activities are not as high as for the noble-metal catalyst at low temperature, at temperatures above 800–900 °C, conversion of methane approaches equilibrium values. For the experimental validation of the C1 and C2 design concept, a SrMnAlO hexa-aluminate catalyst was coated on the metal foam support and placed prior the Rh-section inside the reactor. Under the assumption that the hexa-aluminate performs similar as the Rh-based catalyst, the hexa-aluminate section was sized proportionally to reduce the temperature to about 850 °C before entering the Rh-segment. The volume of the hexa-aluminate coated catalyst section was 23% of the total catalyst section in the ATR.

2.1.2. The water gas shift reactors

Base metal oxide catalysts such as Fe–Cr and Cu–Zn are typically used in the industrial production of H_2. However, these catalysts are designed for steady-state operation with well-controlled start-up and shutdown procedures. Because of our application constraints (e.g., daily start-up and shutdown, high turndown ratios) we chose to use a noble-metal-based catalyst for durability considerations [21]. A precious-metal catalyst, coated on a foam support, was selected for the WGS reactor.

A numerical study was conducted to properly size the WGS reactors. Kinetic information about the commercial catalyst was not available. To estimate the necessary size of the WGS reactors we assumed the kinetics for a shift catalyst based on 1 wt% Pt supported on zirconia-doped ceria derived in a previous work [21,22]. The
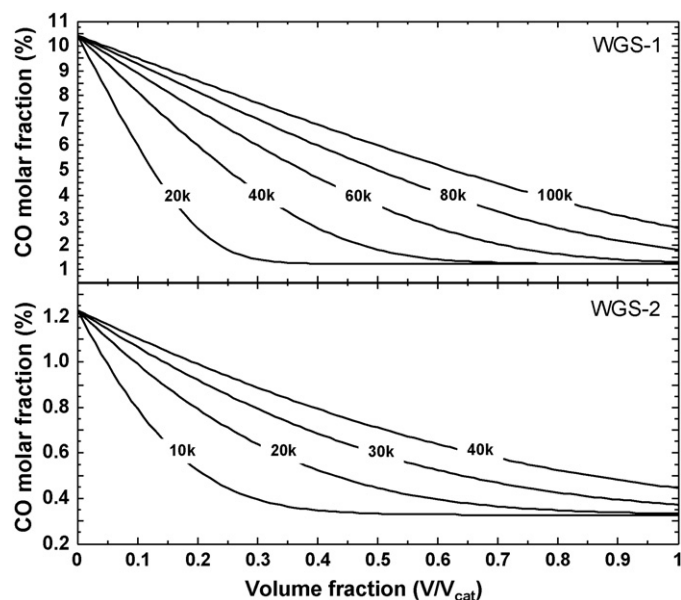

Fig. 7. CO concentration profiles (dry basis) for WGS1 and WGS2 as function of space velocity. Design based on C1 conditions.

kinetics was incorporated into the same model used to size the ATR reactor. Only reaction (4) was used while the other reactions were switched off. Possible methane formation was not accounted for in the kinetic analysis. It was assumed that methane was "frozen" in the WGS unit. We chose C1 conditions to size the WGS reactors (lowest S/C case), used a catalyst loading of 0.15 instead of $0.2\,g\,cm^{-3}$ and sized the reactors at 100% rated capacity to be on the conservative side.

Assuming adiabatic conditions, Fig. 7 shows the calculated concentration profiles of CO for both WGS reactors as functions of space velocity. At the inlet to WGS1, the temperature is 375 °C, the S/C ratio is 4.9, and the CO concentration is 10.4% on a dry basis (exit composition from the ATR at 720 °C). If equilibrium is achieved in the WGS1, the exit temperature should increase to 420 °C and the CO molar fraction should be reduced to 1.25%. The high temperature and S/C ratio temperature will likely promote a very fast reaction. Indeed, at the space velocity of $20,000\,h^{-1}$, the equilibrium concentration of CO is achieved within the first 40% of the catalyst volume, as shown in Fig. 7. Some deviation of the CO concentration from the equilibrium values is observed for space velocities in excess of $60,000\,h^{-1}$.

For WGS2 the inlet temperature is reduced to 300 °C according to the systems model. Assuming that equilibrium conditions have been reached in WGS1, the CO inlet concentration into the second shift reactor is 1.25%. If equilibrium is achieved in WGS2, the CO molar fraction should decrease to 0.3%, while the temperature increases to 304 °C. Despite the lower operating temperature and slower kinetics, a space velocity of $20,000\,h^{-1}$ was still adequate for WGS2 to reduce the CO concentration to nearly equilibrium conditions. The WGS1 and WGS2 reactors were sized for space velocities of $40,000\,h^{-1}$ and $20,000\,h^{-1}$, respectively.

2.1.3. The preferential oxidation reactor

The PrOx reactor(s) were tasked to convert CO from 0.3% (dry) to less than 5 ppm in the reformate to be fed to the fuel cell stack. Based on the kinetics derived for the BASF Selectra® catalyst supported on a Corning 600-cpi cordierite monolith [6], it was estimated that a single-stage unit with a space velocity of $30,000\,h^{-1}$ would be sufficient to achieve the desired conversion.
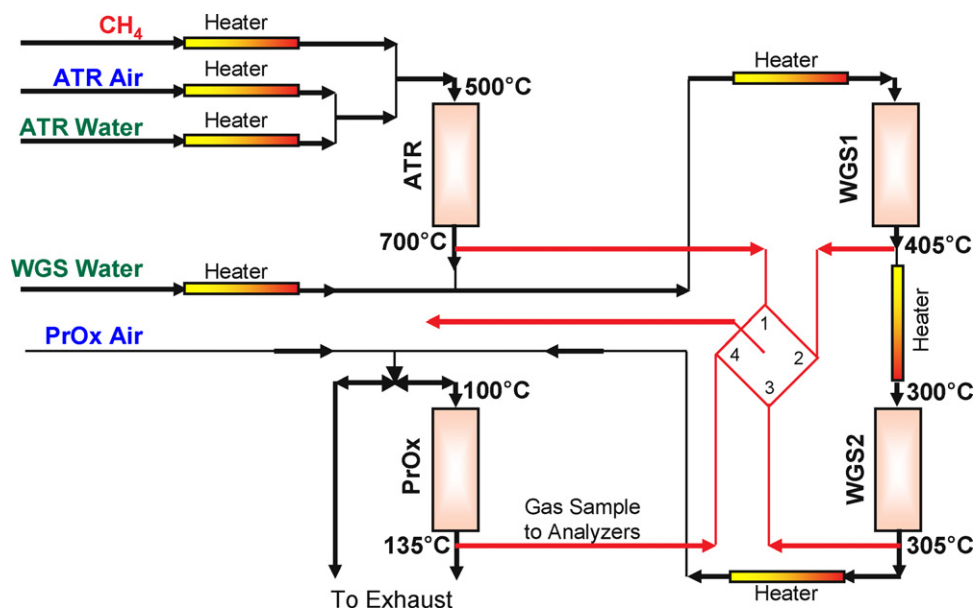
Fig. 8. Simplified schematic of a breadboard apparatus for testing the catalytic reactors in a 1-kWe fuel processor.

3. Evaluation of the catalytic reactors in a breadboard apparatus

A breadboard apparatus was designed and installed to test the catalytic reactors in the fuel processor under both the C1 and C2 sets of conditions. The design and operation of the reactors in the breadboard were similar to that of the fuel cell system configuration discussed earlier (Fig. 1). The breadboard system includes the autothermal reformer, the two stages of the water gas shift reactor (WGS1 and WGS2), and a single-stage preferential oxidation reactor. The catalyst volumes for the respective units are; ATR = 75 cm^3, WGS1 = 87 cm^3, WGS2 = 174 cm^3 and PrOx = 103 cm^3. Fig. 8 shows a high-level schematic of the breadboard system.

Methane, 99.99% pure, from a pressurized cylinder was metered in with a mass flow controller at the requisite rates for each test condition. An electrically heated pre-heater was provided for methane preheating, although the tests reported here used room temperature methane.

The ATR water was pumped in with an HPLC pump to correspond to the desired steam-to-carbon ratio for the ATR. De-ionized water was vaporized and superheated to above 500 °C by passing through an electrically heated steam generator with separate boiler and superheater sections. The steam was bypassed to the exhaust until the reactor was warm enough to prevent condensation.

The ATR air was metered in with a mass flow controller from the house air supply and preheated in an electrical pre-heater to above 500 °C. The preheated streams of air and steam were mixed within an inline static mixer. This mixture and the methane feed were then fed to a second static mixer before being fed into the ATR. Temperatures within the ATR were controlled with the help of the air (oxygen to carbon ratio, O$_2$/C) and the air and steam inlet temperatures.

The reformate from the ATR (~700 °C) was cooled by mixing it with steam supplied to the WGS1 reactor. The mixture of the ATR reformate and steam was then fed to the electrically heated WGS1 pre-heater to maintain the reactant mix at a temperature of about 375 °C as it entered the catalyst bed in the WGS1 reactor.

The reformate leaving the WGS1 (~410 °C) was cooled through the non-heat-traced transport line and then fed into the electrically heated WGS2 pre-heater to maintain ~300 °C at the inlet of the catalyst bed in the WGS2 reactor. The effluent from the WGS2

(~310 °C), was cooled in the non-heat-traced transport line and fed into the electrically heated PrOx pre-heater to maintain a temperature above 100 °C before being combined with the PrOx air that is metered in with a mass flow controller. The product stream from the PrOx reactor was finally vented into the exhaust duct.

To compensate for the heat losses of all feed and process streams, the process flow lines and all four reactors were heat-traced with electrical heating rods and insulated with high-temperature insulation mats. Product gas samples were alternately withdrawn from each of the four reactors. The sample stream was dehumidified by cooling to 2 °C, before passing through the sample loop in an online gas chromatograph. The gas sample from the PrOx reactor was further dried in a drierite bed before being sent to a non-dispersive infrared (NDIR) CO analyzer. Thermocouples located within each reactor and at key junctions within the flow path helped monitor the temperatures.

4. Results and discussion

Table 3 shows the feed parameters for the tests conducted in this study. The column C1 corresponds to the reference system described earlier, with a steam-to-carbon ratio of 1.65 for the ATR. To maintain the ATR exit temperature of approximately 700 °C, the air rate was adjusted to 13.6, which corresponds to an O$_2$/C = 0.52. The water (in the form of steam) added to the WGS1 feed was 13.1 ml min^{-1}, which resulted in a combined S/C of 4.9. The air fed into the PrOx reactor was 0.65, adjusted to reduce the CO level

Table 3
Feed parameters for the experimental study.

Feed/parameter	C1	C2	C2-40%
Methane (slpm)	5.5	5.5	2.25
ATR air (slpm)	13.6	13.9	6.0
O$_2$/C	0.52	0.53	0.57
ATR water (mL min^{-1})	6.7	9.0	3.6
H$_2$O/C	1.65	2.2	2.2
WGS1 water (mL min^{-1})	13.1	13.1	5.2
H$_2$O/C	3.2	3.2	3.2
Combined (FP) H$_2$O/C	4.9	5.4	5.4
PrOx air (slpm)	0.65	0.65	0.26
O$_2$/CO	~1.6	~1.6	~1.6

Table 4
ATR temperatures and gas yields.

Temperature/composition	C1	C2	C2-40%
Temperature, °C – inlet, T_{ATR1}	474	472	466
Temperature, °C – T_{ATR2}	826	807	829
Temperature, °C – T_{ATR3}	721	728	722
Temperature, °C – T_{ATR4}	689	697	655
Yield – H_2, mol/mol-CH_4 (%-dry)	2.41 (44.9)	2.48 (45.3)	2.45 (44.0)
Yield – CO, mol/mol-CH_4 (%-dry)	0.50 (9.4)	0.43 (8.0)	0.39 (6.9)
Yield – CO_2, mol/mol-CH_4 (%-dry)	0.48 (8.9)	0.54 (9.96)	0.59 (10.7)
Yield – CH_4, mol/mol-CH_4 (%-dry)	0.019 (0.36)	0.011 (0.19)	0.019 (0.34)

to less than 5 ppm. Based on the CO concentrations in the WGS2 effluent, the O_2/CO ratio in the PrOx feed was ~1.6.

The condition C2 corresponds to a configuration where the ATR can be operated at a higher steam-to-carbon ratio of 2.2. In order to maintain the ATR exit temperature of 700 °C, the air feed rate had to be increased to 13.9. The C2-40% column reflects the feed rates used to operate at the part-load condition, where the fuel feed rate is 40% of the design rate.

4.1. The autothermal reformer

Table 4 shows the temperatures in the ATR for the three operating conditions. The temperatures are measured at four locations in the axial direction, namely, T_{ATR1}: at the inlet of the hexa-aluminate catalyst (1 mm from the inlet edge of the hexa-aluminate catalyst block); T_{ATR2}: inlet (1 mm) of the rhodium catalyst; T_{ATR3}: 1 mm from the inlet of the second of two rhodium catalyst foam blocks; T_{ATR4}: exit (1 mm from the exit edge) of the second rhodium catalyst. Each temperature value in the table is the average of the readings from four thermocouples located on the radial plane at that axial position. The measurements show the anticipated peak temperature near the bed inlet where the oxygen is rapidly consumed by the exothermic oxidation reaction. This was followed by a gradual temperature decline caused by the net thermal effects of the endothermic steam reforming reaction, the mildly exothermic water gas shift reaction, and the heat loss from the reactor. For the three operating conditions, the difference in the S/C and O_2/C for C1 and C2 conditions do affect the temperatures somewhat. The difference is most noteworthy for the part load condition (C2-40%), where the peak temperature was found to be the highest and the subsequent temperature drop to the exit was the sharpest. This primarily reflects the effect of heat losses and the associated increase in O_2/C ratio. While the total heat loss from the reactor remains essentially the same, at the lower processing rate, it represents a larger fraction of the heat generated. To compensate for the lower temperature near the exit of the reactor, the O_2/C ratio was increased to 0.57. The resulting additional heat generation was successful in raising the exit temperature but also had the undesired effect of increasing the peak temperature at the front of the catalyst section.

Fig. 9 shows the temperature history within the ATR during operation at C1 and C2 conditions. The start-up of the reactor was accomplished by introducing the methane and air into a preheated (by passing hot air through the reactor) catalyst zone. The introduction of steam and methane feeds into the reactor resulted in a sharp drop in temperature at the inlet (T_{ATR1}) and the sharp rises in T_{ATR2}, T_{ATR3}, and T_{ATR3}. The temperatures remained very steady throughout the run. Even the transition from C1 to C2 conditions, where especially the water feed rate was increased significantly, temperature differences between the two cases was found to be quite moderate. The combined effect of the higher S/C, O_2/C and
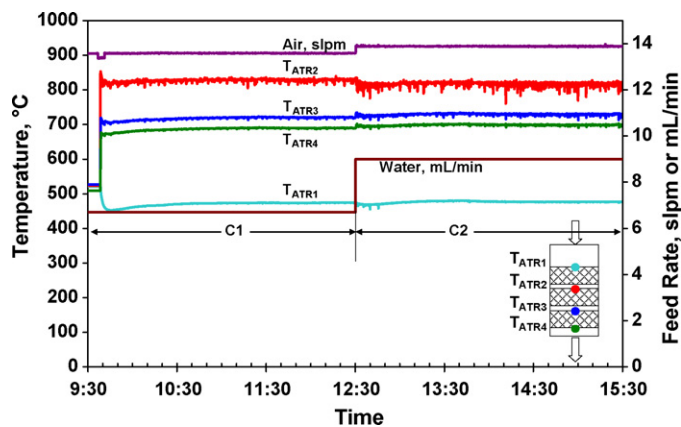

Fig. 9. ATR temperature history during operation at C1 and C2 conditions. Also shown are the corresponding air and liquid water feed rates. The CH_4 feed rate was constant at 5.5 slpm.

space velocity resulting from the transition to C2 condition lowered T_{ATR2} while increasing T_{ATR3} and T_{ATR4}. This trend supports the results of the ATR model in Section 2.1 as shown previously in Figs. 5 and 6. An anticipated decrease in peak temperature of 30 °C was predicted from the transition to C2 conditions, which is in the same order as observed from the experimental results ~20 °C. With increased S/C ratios, the increased space velocity serves to push the hot zone farther downstream (see Fig. 6). This effect, together with the fact that that the relative heat losses decrease at higher feed rates, results in slightly higher downstream temperatures for the C2 condition.

Table 4 shows that the product gas from the ATR contained approximately 45% hydrogen and 9% CO, with a methane conversion of 98% under C1 condition. The higher S/C ratio at C2 condition improved the methane conversion to 99% and also favored the water gas shift reaction ($CO + H_2O = H_2 + CO_2$) as seen in the higher hydrogen and lower CO yields and percentages.

Fig. 10 compares the experimental methane content in the product gas with that predicted from equilibrium (HSC Chemistry) calculations. The experimental CH_4 concentrations approach the equilibrium values for all three conditions, suggesting that the space velocities and temperatures for the reactor are sufficient to provide the needed conversion. The minor variance between the measured and predicted values may be attributed to the difference in the measured temperatures and the actual average temperatures of the exit gases. It is notable that for the test at 40%-C2 condition, where the heat loss represented a larger fraction of the heat content,
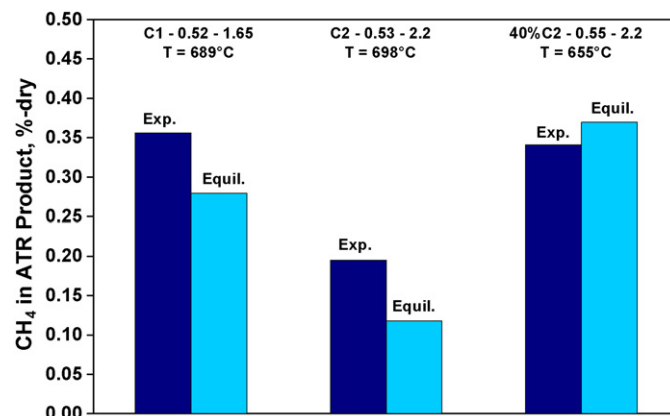

Fig. 10. Comparison of the measured and equilibrium predicted methane concentration in the ATR product gas.
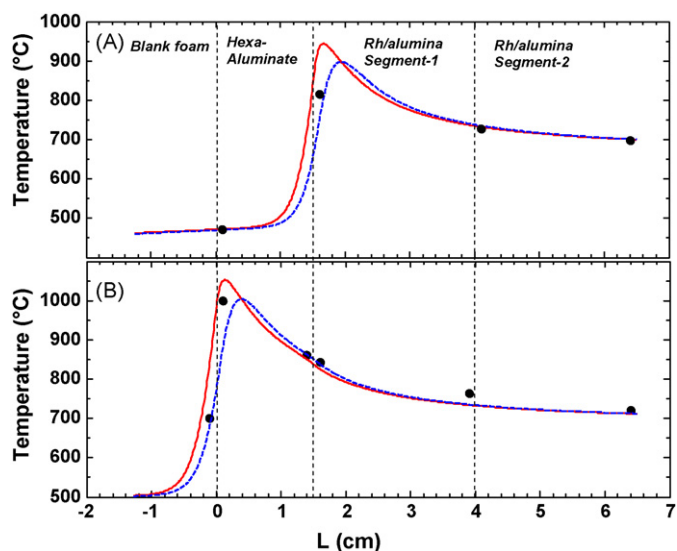
Fig. 11. ATR measured and modeled axial temperature profiles. (A) C2 conditions and (B) C1 conditions at 80% part load and inlet temperature of 505 °C. Solid and dashed lines denote solid- and gas-phase temperature. Symbols denote measured temperatures.

the exit temperature was almost 45 °C cooler (compared to C2 condition) and the equilibrium-predicted methane content increases by more than a factor of two. This illustrates the importance of the ATR exit temperature on methane conversion.

4.1.1. Dual catalyst bed performance

Under most conditions investigated, the hexa-aluminate catalyst layer having a much lower activity than Rh was inactive and reforming reactions took place on the noble-metal catalyst layer. By increasing the inlet temperature and lowering the space velocity, however, the fast oxygen consumption and associated spike in temperature shifted from the Rh catalyst and took place near the hexa-aluminate front section. Fig. 11 shows axial temperature profiles in the ATR for two experimental conditions: (A) C2 conditions where oxidation reactions occur on the Rh catalyst and (B) C1 conditions at 80% part load and inlet temperature of 505 °C, conditions that shifted the oxidation reactions from the rhodium to the hexa-aluminate section. The solid and broken lines are calculated solid- and gas-phase temperature respectively while the symbols denote measured temperature profiles (average values in the radial plane). For the experiments in case B, thermocouples were repositioned to provide more axial points between the catalyst segments. The probes were positioned 1-mm deep at each end of the catalyst segments.

Given experimental uncertainties for the exact location of the thermocouple and the difficulty to measure solid temperatures, the model manages to predict the experimental temperatures adequately for both cases. For the peak temperature, when the solid temperature exceeds the gas-phase temperature, the experimental data point seems to be closer to the gas-phase temperature. The modeled results indicate the danger of excessive solid temperature and risk of deactivation for the noble-metal catalyst. Kinetic information for the hexa-aluminate catalyst was not available and the same reaction rates as the Rh-catalyst were assumed. Kinetic rates were turned on or off on the hexa-aluminate in order to model the two distinct cases. The good agreement with the experimental temperature profiles for case B indicates that the reaction is transport limited at these high temperatures. Oxygen is completely consumed in the hexa-aluminate section and over 80% of methane is converted before entering the Rh-section. Although the measured temperature at the inlet of the Rh section is sim-

Table 5
WGS1 temperatures and gas yields.

Temperature/composition	C1	C2	C2-40%
Temperature, °C – T_{WGS11}	366	371	353
Temperature, °C – T_{WGS12}	409	401	380
Temperature, °C – T_{WGS13}	409	405	377
Temperature, °C – T_{WGS14}	406	403	371
Yield – H_2, mol/mol-CH_4 (%-dry)	2.86 (49.2)	2.85 (48.8)	2.80 (47.3)
Yield – CO, mol/mol-CH_4 (%-dry)	0.046 (0.80)	0.038 (0.66)	0.027 (0.46)
Yield – CO_2, mol/mol-CH_4 (%-dry)	0.93 (15.9)	0.94 (16.0)	0.95 (16.0)
Yield – CH_4, mol/mol-CH_4 (%-dry)	0.027 (0.47)	0.017 (0.29)	0.023 (0.38)

ilar for both the cases, the model temperature profiles show a very important distinction. In case A, where the peak temperature is located in the Rh-catalyst, the solid temperature significantly exceeds the gas-phase temperature. In case B, oxygen has been consumed at the front of the hexa-aluminate layer with associated spike in solid temperature. The solid- and gas-phase temperature approach thermal equilibrium at the entrance of the Rh-layer. A further decrease in temperature at the inlet of the Rh-layer can be realized by increasing the volume of the hexa-aluminate catalyst.

4.2. First stage water gas shift reactor (WGS1)

The reformate from the ATR was mixed with steam to cool the reformate from 700 °C and to increase the S/C to favor the conversion of CO in the water gas shift reactors. The inlet temperature into the first stage (WGS1) was controlled to ~375 °C. More than 90% of the CO from the ATR was converted in WGS1 and the reformate temperature was raised by ~30 °C, the latter being the net result of the heat of reaction and heat losses. These results are summarized in Table 5. The temperatures were measured at the centerline, with T_{WGS11} at the inlet and T_{WGS12} at the exit of the first catalyst block. Fig. 12 shows the temperature history within the WGS1 reactor. The sharp rise in temperature between T_{WGS11} and T_{WGS12}, followed by the nearly identical temperatures at T_{WGS12}, T_{WGS13}, and T_{WGS14} suggests that the majority of the CO conversion that occurs in this reactor takes place within the first catalyst block.

In order to validate the kinetic model for the water gas shift catalyst, the experimentally measured axial temperature and the CO concentration profile was compared to that calculated from the model discussed earlier (Section 2.1, Fig. 7). With an inlet temperature of 375 °C, the reaction rate was very fast which led to the experimental attainment and calculated prediction of equilibrium
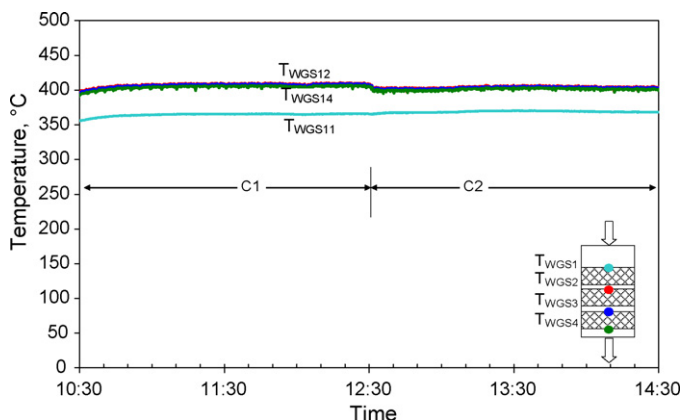

Fig. 12. Temperature history within WGS1 for operations at C1 and C2 conditions.
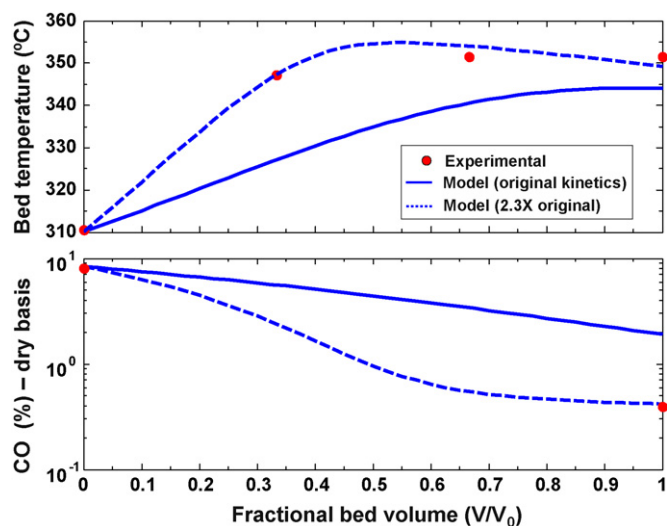
Fig. 13. Comparison of the measured and calculated (reactor model) temperature and CO concentrations from the WGS1 reactor.

conversion under essentially adiabatic condition. As such the experimental and calculated numbers matched very closely. However, when the inlet temperature of that same reformate was lowered to 310 °C, the predicted concentration and temperature profiles were found to be considerably lower than the measured values. However, by adjusting the kinetic expression with an Arrhenius constant that is 2.3 times the original value, the model was able to match the experimental values much more closely. The comparison of the experimental data points with the predicted values using the original (solid line) and the revised (dotted line) kinetic expressions are shown in Fig. 13.

4.3. Second stage water gas shift reactor (WGS2)

The second water gas shift reactor, the largest of the four reactors, was operated with a reformate inlet temperature of ~300 °C. The measured temperatures and product yields are reported in Table 6, which shows that the CO levels can be reduced to less than 0.3%, converting 39% of the inlet CO at C1 and C2 conditions, and 48% at the part load condition. The higher conversion at the 40%-C2 condition is a result of the longer residence time within the reactor and lower exit temperatures. Fig. 14 shows the temperature history at the centerline of WGS2. The temperatures at the four axial points (T_{WGS21}, T_{WGS22}, T_{WGS23}, and T_{WGS24}) remained fairly constant and this may be anticipated since the actual mols of CO being converted inside the reactor is about an order of magnitude smaller than that achieved in WGS1.

Table 6
WGS2 temperatures and gas yields.

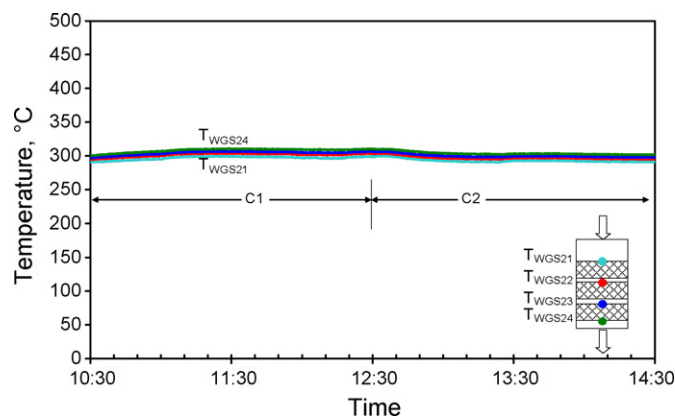| Temperature/composition	C1	C2	C2-40%
Temperature, °C – T_{WGS21}	299	294	246
Temperature, °C – T_{WGS22}	304	298	260
Temperature, °C – T_{WGS23}	306	301	283
Temperature, °C – T_{WGS24}	310	305	298
Yield – H_2, mol/mol-CH_4 (%-dry)	2.87 (49.3)	2.88 (49.1)	2.80 (47.2)
Yield – CO, mol/mol-CH_4 (%-dry)	0.018 (0.30)	0.015 (0.25)	0.013 (0.21)
Yield – CO_2, mol/mol-CH_4 (%-dry)	0.95 (16.3)	0.96 (16.4)	0.96 (16.3)
Yield – CH_4, mol/mol-CH_4 (%-dry)	0.028 (0.48)	0.015 (0.26)	0.025 (0.43)

Fig. 14. Temperature history within WGS2 for operations at C1 and C2 conditions.

4.4. The preferential oxidation reactor

The reformate from the WGS2 along with air was processed through a single stage preferential oxidation (PrOx) reactor. With the reformate containing 0.25% CO, the air feed into the reactor corresponded to a O_2/CO molar ratio of 1.62. Entering at ~100 °C, the reformate temperature rose sharply to ~130 °C after the first monolith catalyst. It is likely that the oxygen was completely consumed within the first monolith. The temperature rise in the second catalyst was less than 5 °C and was most likely the result of the methanation reaction. The air feed rate and the temperature history within the reactor for the C2 conditions are shown in Fig. 15. The on-line infrared CO analyzer indicated that the CO levels were less than 5 ppm. Methane analyzed with the GC, revealed slightly higher methane content at the exit of the PrOx reactor.

Mass balance calculations were set up for the preferential oxidation reactor and the exit yields of H_2, CO, CO_2, and CH_4 were calculated based on an assumed value for the percentage of the mols of inlet CO that reacted with oxygen (CO selectivity, S_{CO}). It is assumed that the balance of CO reacts with H_2 to form CH_4.

$$S_{CO} = \frac{n_{CO \to CO_2}}{n_{CO,in,exp}} \times 100 \qquad (7)$$

where $n_{CO \to CO_2}$ is the mols of CO assumed to react with oxygen to form CO_2 and $n_{CO,in,exp}$ is the experimentally measured mols of CO entering the reactor. Knowing S_{CO} permits the calculation of the moles of the other species leaving the reactor. The parameter S_{CO} was then adjusted to minimize the sum of squares of the errors between the calculated and experimental yields of H_2, CO, CO_2, and
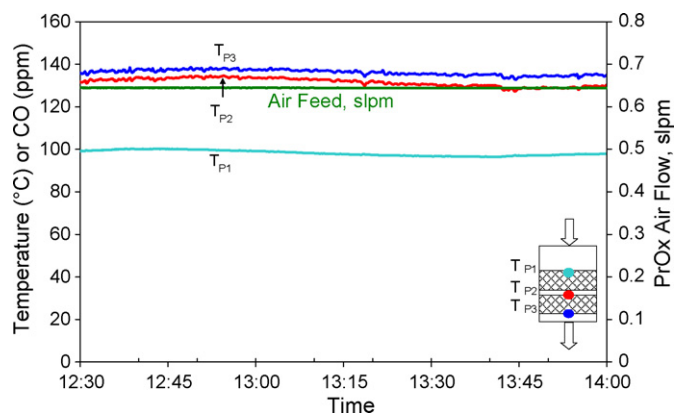

Fig. 15. Temperature history in the preferential oxidation reactor during operation at C2 conditions.

Table 7
Results from the PrOx.

	C1	C2
PrOx air feed (slpm)	0.64	0.64
O_2/CO at PrOx inlet	1.61	1.63
In/out temperature (°C)	99/133	98/134
Yield – H_2, mol/mol-CH_4 (%-dry)	2.84 (48.2)	2.82 (47.7)
Yield – CO, mol/mol-CH_4 (%-dry)	0	0
Yield – CO_2, mol/mol-CH_4 (%-dry)	0.97 (16.5)	0.98 (16.6)
Yield – CH_4, mol/mol-CH_4 (%-dry)	0.028 (0.48)	0.016 (0.26)
CO oxidized, % of inlet CO (balance to CH_4 formation)	97%	99%
O_2 reacting with CO, % of inlet O_2 (balance to H_2 oxidation)	30%	31%
H_2 loss, % of H_2 entering PrOx	1.8%	1.7%

CH_4. The error function (E) was defined as

$$E = \sum_j \left(\frac{n_{j,\text{out,exp}} - n_{j,\text{out,cal}}}{n_{j,\text{in,exp}}} \right)^2 \qquad (8)$$

where $n_{j,\text{out,exp}}$ refers to the experimentally measured number of mols of species j leaving the reactor, $n_{j,\text{out,cal}}$ the calculated number of mols of species j leaving the reactor, and $n_{j,\text{in,exp}}$ is the experimentally measured number of mols of species j entering the reactor, and j refers to H_2, CO, CO_2, and CH_4.

The selectivity (S_{CO}) value that most closely fitted the data was found to vary between 97 and 99%, indicating that the oxidation reaction was the dominant reaction for the conversion of CO, with only the remaining small fraction being converted by the methanation reaction. Of the oxygen that was fed into the reactor, 30–31% was consumed in the oxidation of CO, the balance (69–70%) reacting with hydrogen. Of the hydrogen entering the PrOx, 1.7–1.8% was lost due to oxidation and methanation reactions. These results are summarized in Table 7.

4.5. Overall performance

The methane feed to the catalytic reactors in the breadboard produced a final product that contained 48% hydrogen, on a dry basis, with a hydrogen yield of 2.8 mol/mol of methane. The overall methane conversion in the reactors was 98.2%. The two stages of the shift reactor and the preferential oxidation reactor were able to reduce the CO level from 9.4% at the ATR exit to less than 5 ppm, low enough to be suitable for the reformate-fueled polymer electrolyte fuel cell.

A closer look into the product yields as the reformate progressed through the reactors shows that the methane content increased downstream from the ATR. The most significant contribution, as seen in Fig. 16, was within the WGS1 reactor where the temperatures ranged from 360 to 410 °C. This is somewhat anticipated considering that the platinum-based catalyst has been reported to promote the methanation reaction [23,24]. Considering that the conversion of methane is an important metric for the ATR design and considerable effort is directed towards achieving that objective, the formation of methane in downstream reactors should be avoided if possible. By the same token, it should be pointed out that the reformate-based fuel cell stacks do not consume all of the hydrogen. The unreacted hydrogen, along with the methane, is combusted in the spent fuel burner to generate steam or to preheat the feeds. As such, the minor loss in hydrogen yield that results from the presence of a small quantity of methane in the anode feed may easily be "acceptable". The limit for "acceptable" methane content
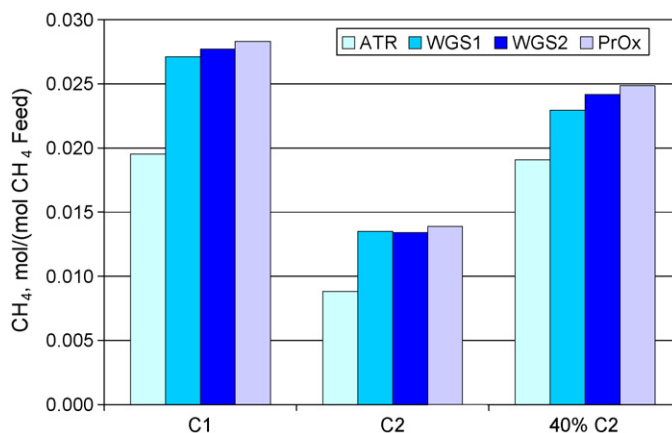

Fig. 16. Methane yields from the catalytic reactors.

should ultimately be determined from the perspective of the efficiency calculations for the overall fuel cell system that also includes the fuel processor.

5. Conclusions

An ATR-based fuel processing system has been designed for a residential fuel cell system to meet the targets for efficiency (>80% HHV) and start-up energy (<1 kWh per start). The key catalytic reactors were designed, fabricated, and then tested in a breadboard apparatus that processed 5.5 slpm (∼1 kWe) of methane. It was shown that a dual catalyst bed in the ATR, with a leading hexa-aluminate section, can help limit the peak temperature exposure on the precious metal catalyst that follows. The experimental results showed that the ATR could convert over 98% of the methane, that two stages of the water gas shift reactor could reduce the CO levels to less than 0.3% (dry), with a hydrogen concentration greater than 49% (dry). The non-optimized single stage preferential oxidation reactor was able to reduce the CO levels to below 5 ppm, with a CO selectivity greater than 30%. Some methanation reaction was observed in the first water gas shift reactor. A modeling analysis based on the fuel cell system (since it includes the post-fuel cell burner which generates heat recoverable by the fuel processor) can be an effective approach to determine the impact of this methane formation and what, if any, changes in the WGS1 operating temperature and/or space velocity would be meaningful from the application goals of system efficiency, weight (start-up energy), and cost.

References

[1] T. Omata, T. Kimura, Y. Yamamoto, S. Nishikawa, Fuel Cell Seminar Abstracts, San Antonio, TX, 2007, pp. 59–62.

[2] T. Iseki, T. Bessho, Fuel Cell Seminar Abstracts, San Antonio, TX, 2007, pp. 277–280.
[3] S. Ahmed, R. Ahluwalia, S.H.D. Lee, S. Lottes, J. Power Sources 154 (2006) 214–222.
[4] H.K. Geyer, R.K. Ahluwalia, GCTool for Fuel Cell Systems Design and Analysis: User Documentation, Argonne National Laboratory, Report ANL-98/8, 2005.
[5] R.K. Ahluwalia, X.H. Wang, J. Power Sources 177 (2008) 167–176.
[6] R.K. Ahluwalia, Q.Z. Zhang, D.J. Chmielewski, K.C. Lauzze, M.A. Inbody, Catal. Today 99 (2005) 271–283.
[7] M. Ferrandon, T. Krause, Appl. Catal. A: Gen. 311 (2006) 135–145.
[8] V.V. Calmidi, R.L. Mahajan, J. Heat Trans. 122 (2000) 557–565.
[9] L. Giani, G. Groppi, E. Tronconi, Ind. Eng. Chem. Res. 44 (2005) 4993–5002.
[10] D. Papadias, S.H.D. Lee, D.J. Chmielewski, Ind. Eng. Chem. Res. 45 (2006) 5841–5858.
[11] L. Giani, G. Groppi, E. Tronconi, Ind. Eng. Chem. Res. 44 (2005) 9078–9085.
[12] I. Tavazzi, M. Maestri, A. Beretta, G. Groppi, E. Tronconi, P. Forzatti, AIChE J. 52 (2006) 3234–3245.
[13] I. Tavazzi, A. Beretta, G. Groppi, M. Maestri, E. Tronconi, P. Forzatti, Catal. Today 129 (2007) 372–379.
[14] R. Kikuchi, Y. Tanaka, K. Sasaki, K. Eguchi, Catal. Today 83 (2003) 223–331.
[15] P. Forzatti, Catal. Today 83 (2003) 3–18.
[16] E.M. Johansson, D. Papadias, O.P. Thevenine, A.G. Ersson, R. Gabrielsson, P.G. Menon, P.H. Björnbom, S.G. Järås, in: J.J. Spivey (Ed.), Catalysis, The Royal Society of Chemistry, Cambridge, 1999, pp. 183–235.
[17] T. Utaka, S.A. Al-Drees, J. Ueda, Y. Iwasa, T. Takeguchi, R. Kikuchi, K. Eguchi, Appl. Catal. A: Gen. 247 (2003) 125–131.
[18] W. Chu, W. Yang, L. Lin, Appl. Catal. A: Gen. 235 (2002) 39–46.
[19] R. Kikuchi, Y. Iwasa, T. Takeguchi, K. Eguchi, Appl. Catal. A: Gen. 281 (2005) 61–67.
[20] L. Majocchi, G. Groppi, C. Cristiani, P. Forzatti, L. Basini, A. Guarinoni, Catal. Lett. 65 (2000) 49–56.
[21] S.Y. Choung, M. Ferrandon, T. Krause, Catal. Today 99 (2005) 257–262.
[22] D. Papadias, S.Y. Choung, T. Krause, AIChE Annual Meeting Proceedings, Austin, TX, 2004.
[23] C. Wheeler, A. Jhalani, E.J. Klein, S. Tummala, L.D. Schmidt, J. Catal. 223 (2004) 191–199.
[24] C.M.Y. Yeung, F. Meunier, R. Burch, D. Thompsett, S.C. Tsang, J. Phys. Chem. B 110 (2006) 8540–8543.